

## Accelerated Article Preview

# Light Curves and Colors of the Ejecta from Dimorphos after the DART Impact

---

Received: 6 November 2022

---

Accepted: 15 February 2023

---

Accelerated Article Preview

---

Cite this article as: Graykowski, A. et al. Light Curves and Colors of the Ejecta from Dimorphos after the DART Impact. *Nature* <https://doi.org/10.1038/s41586-023-05852-9> (2023)

---

Ariel Graykowski, Ryan A. Lambert, Franck Marchis, Dorian Cazeneuve, Paul A. Dalba, Thomas M. Esposito, Daniel O'Conner Peluso, Lauren A. Sgro, Guillaume Blaclard, Antonin Borot, Arnaud Malvache, Laurent Marfisi, Tyler M. Powell, Patrice Huet, Matthieu Limagne, Bruno Payet, Colin Clarke, Susan Murabana, Daniel Chu Owen, Ronald Wasilwa, Keiichi Fukui, Tateki Goto, Bruno Guillet, Patrick Huth, Satoshi Ishiyama, Ryuichi Kukita, Mike Mitchell, Michael Primm, Justus Randolph, Darren A. Rivett, Matthew Ryno, Masao Shimizu, Jean-Pierre Toullec, Stefan Will, Wai-Chun Yue, Michael Camilleri, Kathy Graykowski, Ron Janetzke, Des Janke, Scott Kardel, Margaret Loose, John W. Pickering, Barton A. Smith & Ian M. Transom

---

This is a PDF file of a peer-reviewed paper that has been accepted for publication. Although unedited, the content has been subjected to preliminary formatting. Nature is providing this early version of the typeset paper as a service to our authors and readers. The text and figures will undergo copyediting and a proof review before the paper is published in its final form. Please note that during the production process errors may be discovered which could affect the content, and all legal disclaimers apply.

# 1 **Light Curves and Colors of the Ejecta from Dimorphos after the DART** 2 **Impact**

3 Ariel Graykowski<sup>1</sup>, Ryan A. Lambert<sup>1</sup>, Franck Marchis<sup>1,2</sup>, Dorian Cazeneuve<sup>1</sup>, Paul A.  
4 Dalba<sup>1,3,4</sup>, Thomas M. Esposito<sup>1,2,5</sup>, Daniel O’Conner Peluso<sup>1,6</sup>, Lauren A. Sgro<sup>1,2</sup>, Guillaume  
5 Blaclard<sup>2</sup>, Antonin Borot<sup>2</sup>, Arnaud Malvache<sup>2</sup>, Laurent Marfisi<sup>2</sup>, Tyler M. Powell<sup>7</sup>, Patrice  
6 Huet<sup>8</sup>, Matthieu Limagne<sup>9</sup>, Bruno Payet<sup>10</sup>, Colin Clarke<sup>11,12,13</sup>, Susan Murabana<sup>12,14</sup>, Daniel  
7 Chu Owen<sup>12,14</sup>, Ronald Wasilwa<sup>12,14</sup>, Keiichi Fukui<sup>15</sup>, Tateki Goto<sup>16</sup>, Bruno Guillet<sup>17</sup>, Patrick  
8 Huth<sup>18,19</sup>, Satoshi Ishiyama<sup>20</sup>, Ryuichi Kukita<sup>21</sup>, Mike Mitchell<sup>22</sup>, Michael Primm<sup>23</sup>, Justus  
9 Randolph<sup>24</sup>, Darren A. Rivett<sup>25</sup>, Matthew Ryno<sup>26</sup>, Masao Shimizu<sup>27</sup>, Jean-Pierre Toullec<sup>28</sup>,  
10 Stefan Will<sup>29</sup>, Wai-Chun Yue<sup>30</sup>, Michael Camilleri<sup>31</sup>, Kathy Graykowski<sup>32</sup>, Ron Janetzke<sup>33</sup>, Des  
11 Janke<sup>34</sup>, Scott Kardel<sup>35,36</sup>, Margaret Loose<sup>37</sup>, John W. Pickering<sup>38,39,40</sup>, Barton A. Smith<sup>41</sup>, Ian  
12 M. Transom<sup>42,43</sup>

13  
14 Corresponding Email: [agraykowski@seti.org](mailto:agraykowski@seti.org)

15 <sup>1</sup>SETI Institute, Carl Sagan Center, 339 Bernardo Ave Suite 200, Mountain View, 94043, CA,  
16 USA

17 <sup>2</sup>Unistellar, 5 allée Marcel Leclerc, Bâtiment B., Marseille, 13008, France

18 <sup>3</sup>Department of Astronomy and Astrophysics, University of California, Santa Cruz, 95064, CA,  
19 USA

20 <sup>4</sup>Heising-Simons 51 Pegasi b Postdoctoral Fellow

21 <sup>5</sup>Astronomy Department, University of California, Berkeley, 94720, CA, USA

22 <sup>6</sup>Centre for Astrophysics, University of Southern Queensland, Toowoomba, QLD, Australia

23 <sup>7</sup>Department of Earth, Planetary, and Space Sciences, University of California, Los Angeles,  
24 90095, CA, USA

25 <sup>8</sup>Unistellar Citizen Scientist, Le Tampon, France

26 <sup>9</sup>Unistellar Citizen Scientist, Saint-Paul, Réunion

27 <sup>10</sup>Unistellar Citizen Scientist, La Rivière, Réunion

28 <sup>11</sup>Armagh Observatory and Planetarium, College Hill, Armagh BT61 9DB, United Kingdom

29 <sup>12</sup>The Travelling Telescope, Nairobi Planetarium, Kenya

30 <sup>13</sup>Unistellar Citizen Scientist, College Hill, United Kingdom

31 <sup>14</sup>Unistellar Citizen Scientist, Nairobi, Kenya

32 <sup>15</sup>Unistellar Citizen Scientist, Tsuchiura, Japan

- 33 <sup>16</sup>Unistellar Citizen Scientist, Osaka, Japan
- 34 <sup>17</sup>Unistellar Citizen Scientist, Caen, France
- 35 <sup>18</sup>Community College of Allegheny County, 800 Allegheny Ave #1804, Pittsburgh, 15233, PA,  
36 USA
- 37 <sup>19</sup>Unistellar Citizen Scientist, Schenley, PA, USA
- 38 <sup>20</sup>Unistellar Citizen Scientist, Chigasaki, Japan
- 39 <sup>21</sup>Unistellar Citizen Scientist, Kajiki Aira, Japan
- 40 <sup>22</sup>Unistellar Citizen Scientist, Oklahoma City, OK, USA
- 41 <sup>23</sup>Unistellar Citizen Scientist, Austin, TX, USA
- 42 <sup>24</sup>Unistellar Citizen Scientist, Athens, GA, USA
- 43 <sup>25</sup>Unistellar Citizen Scientist, Lake Macquarie, Australia
- 44 <sup>26</sup>Unistellar Citizen Scientist, Milwaukee, WI, USA
- 45 <sup>27</sup>Unistellar Citizen Scientist, Shimoishii, Japan
- 46 <sup>28</sup>Unistellar Citizen Scientist, Saint-Gilles, Réunion
- 47 <sup>29</sup>Unistellar Citizen Scientist, Raleigh, NC, USA
- 48 <sup>30</sup>Unistellar Citizen Scientist, Hong Kong
- 49 <sup>31</sup>Unistellar Citizen Scientist, Auckland, New Zealand
- 50 <sup>32</sup>Unistellar Citizen Scientist, San Francisco, CA, USA
- 51 <sup>33</sup>Unistellar Citizen Scientist, San Antonio, TX, USA
- 52 <sup>34</sup>Unistellar Citizen Scientist, Queensland, Australia
- 53 <sup>35</sup>Palomar Community College, San Marcos, 92069, CA, USA
- 54 <sup>36</sup>Unistellar Citizen Scientist, San Marcos, CA, USA
- 55 <sup>37</sup>Unistellar Citizen Scientist, San Diego, CA, USA
- 56 <sup>38</sup>Department of Medicine, University of Otago, Christchurch, New Zealand
- 57 <sup>39</sup>Emergency Care Foundation, Christchurch Hospital, Christchurch, New Zealand
- 58 <sup>40</sup>Unistellar Citizen Scientist, Christchurch, New Zealand
- 59 <sup>41</sup>Unistellar Citizen Scientist, Campbell, CA, USA

60 <sup>42</sup>Hamilton Astronomical Society Observatory, 183 Brymer Road, Rotokauri, Hamilton, 3200,  
61 New Zealand

62 <sup>43</sup>Unistellar Citizen Scientist, Cambridge, New Zealand

63

64 **On 26 September 2022 the Double Asteroid Redirection Test (DART) spacecraft**  
65 **impacted Dimorphos, a satellite of the asteroid 65803 Didymos<sup>1</sup>. Because it is a binary**  
66 **system, it is possible to determine how much the orbit of the satellite changed, as part of a**  
67 **test of what is necessary to deflect an asteroid that might threaten Earth with an impact.**  
68 **In nominal cases, pre-impact predictions of the orbital period reduction ranged from  $\sim 8.8$**   
69  **$- 17.2$  minutes<sup>2,3</sup>. Here we report optical observations of Dimorphos before, during and**  
70 **after the impact, from a network of citizen science telescopes across the world. We find a**  
71 **maximum brightening of  $2.29 \pm 0.14$  mag upon impact. Didymos fades back to its pre-**  
72 **impact brightness over the course of  $23.7 \pm 0.7$  days. We estimate lower limits on the mass**  
73 **contained in the ejecta, which was  $0.3 - 0.5$  % Dimorphos' mass depending on the dust size.**  
74 **We also observe a reddening of the ejecta upon impact.**

75 Four Unistellar eVscopes captured observations of Didymos during the DART impact  
76 into Dimorphos on the night of 26 September 2022. Of all telescopes that observed the DART  
77 impact, from the ground and space, the eVscopes were among the smallest with apertures of 112  
78 mm. Three eVscopes were located on Réunion Island and one in Nairobi, Kenya. Figure 1 shows  
79 eVscope images taken before and after the impact as well as the ejecta produced by the impact.  
80 We observe a fast-moving ejecta plume moving eastward on the plane of the sky and spreading  
81 over a timescale of minutes, as well as slower moving ejecta that morphologically appear to have  
82 formed a coma.

83 Of the four eVscope data sets that included the moment of impact, three were suitable for  
84 photometric analysis because the observers recorded dark frames for image calibration. Thus, we  
85 conducted aperture photometry on these three data sets through a circular aperture radius of 13.6"  
86 or 750 km at the distance of Didymos. The resulting apparent magnitudes measured over time are  
87 displayed in Figure 2.

88 Using data from the eVscopes located in L'Étang-Salé and Saint-Paul, Réunion, we  
89 calculate an impact time of UTC 23:15:02  $\pm$  4 s on 2022 Sep 26, which agrees with the reported  
90 Earth-observed impact time of 23:15:02.183 UTC <sup>1</sup>, itself coming 38 seconds after the actual  
91 time of impact on the spacecraft due to light-travel time (private communication with Julie  
92 Bellerose). Before the impact, we use the observations taken with the eVscope located in L'Étang-  
93 Salé, Réunion to measure an apparent visual magnitude,  $m_v = 14.48 \pm 0.11$  and a minimum  
94 magnitude (maximum brightness)  $m_v = 12.18 \pm 0.03$ . As the fast-moving ejecta moved out of  
95 the photometric aperture, the magnitude increased to  $m_v = 12.96 \pm 0.04$ . At a geocentric distance  
96 of 0.076 au, a heliocentric distance of 1.05 au, and a phase angle of 53.28° at the time of impact,  
97 these correspond to absolute visual magnitudes of  $H_v = 18.12 \pm 0.11$ ,  $15.83 \pm 0.03$ , and  $16.61 \pm$   
98  $0.04$  respectively.

99 We estimate the effective mass in the fast-moving ejecta by calculating the change in  
100 effective cross sections corresponding to magnitudes  $H_v = 15.83 \pm 0.03$  and  $16.61 \pm 0.04$ , and  
101 assuming an average density and albedo for Dimorphos. This is further detailed in the “Mass of  
102 the Ejecta” section of the Methods. We must also assume an average particle radius, so we  
103 consider several scenarios.

104 To begin with, the particles must be small as evidenced by the long tail that developed in  
105 the anti-solar direction several days after impact. We approximate an antisolar tail length of  $\sim 7$   
106  $\times 10^3$  km on the plane of the sky  $\sim 113.7$  hours after impact as shown in Figure 1. Measurements  
107 from the 4.1-meter Southern Astrophysical Research (SOAR) Telescope, at NSF NOIRLab's  
108 Cerro Tololo Inter-American Observatory in Chile revealed the tail length to be  $>10^4$  km on the  
109 plane of the sky two days after impact<sup>4</sup>. Our measurement is shorter due to the smaller collecting  
110 area of the eVscope and its lesser sensitivity to low surface brightness. We measure a  $3\sigma$  limiting  
111 magnitude of  $17.01 \pm 0.03$  in this image stack consisting of 1,205 four-second exposures.

112 We then refer to active asteroid (596) Scheila, whose activity was likely caused by an  
113 impact and whose average ejected dust size is predicted to be small based on the observed effect  
114 of solar radiation sweeping<sup>5</sup>. From this, average dust radii spanning  $\bar{a} \sim 0.1 - 1.0 \mu\text{m}$  were  
115 estimated. We point out that larger dust sizes were also estimated for Scheila such as  $\bar{a} \sim 100$   
116  $\mu\text{m}$  based on a modeled particle range of  $a \sim 1$  to  $\sim 10^4 \mu\text{m}$  along a power-law distribution with  
117 an index  $q = 3.5^{6,7}$ .

118 We first examine an average particle radius  $\bar{a} \sim 1 \mu\text{m}$ , as particles much smaller than this  
119 become less efficient at scattering visible light, and particles much larger than this are expected  
120 to persist longer in the photometric aperture. This particle radius then results in a mass of  $m_{fe} \sim$   
121  $(7.0 \pm 1.2) \times 10^3$  kg contained in the fast-moving ejecta plume respectively. We measured the  
122 speed of this fast-moving ejecta on the plane of the sky through the photometry aperture and find  
123 this fast-moving ejecta has a speed of  $v_{fe} \sim 970 \pm 50 \text{ m s}^{-1}$ . The resulting mass then corresponds  
124 to a kinetic energy of  $KE_{fe} \sim (3.3 \pm 0.6) \times 10^9$  J. The relative kinetic energy of the DART  
125 spacecraft at the time of impact is  $KE_D \sim (1.094 \pm 0.001) \times 10^{10}$  J<sup>1</sup>. This implies that the

126 observed fast-moving ejecta plume carried away  $\sim 30 \pm 6\%$  of the kinetic energy delivered by the  
127 DART spacecraft. This is comparable to impact simulations, which have shown that kinetic  
128 energy can be transferred from the impactor to the ejecta on the order of tens of percent<sup>8, 9, 10</sup>.  
129 Average particle sizes an order of magnitude larger than this would exceed the kinetic energy  
130 introduced by the DART spacecraft, so we do not further consider larger particles sizes as making  
131 up a significant portion of the observed fast-moving ejecta plume. The lower end of the dust size  
132 estimations based on solar radiation pressure,  $\bar{a} \sim 0.1 \mu\text{m}$ , results in an estimated mass of  $m_{\text{fe}} \sim$   
133  $(7.0 \pm 1.2) \times 10^2 \text{ kg}$ , corresponding to  $\sim 3.0 \pm 0.6\%$  of DART's kinetic energy. These values likely  
134 represent underestimates on ejecta mass, given the assumed average dust radii, as only the  
135 particles with velocities high enough to escape Dimorphos ( $v > v_e \sim 0.087 \pm 0.01 \text{ m s}^{-1}$ ) will  
136 contribute to the measurable increase in cross section<sup>1, 11, 12</sup>.

137 To estimate the mass of ejecta contained within the coma, we measure Didymos' fading  
138 rate. The absolute magnitudes of Didymos after impact are plotted in Figure 3. An error-weighted  
139 linear fit indicates that it took  $\sim 23.7 \pm 0.7$  days for the dust to move out of the photometric  
140 aperture with velocity  $v_{ce} \sim 0.37 \pm 0.01 \text{ m s}^{-1}$ . We use an approximated impact relation (Equation  
141 6 in Methods)<sup>13</sup> to relate this with the mass, density, and speed of the DART impactor, and  
142 estimate the mass contained in the coma that resulted from the impact to be  $m_{ce} \sim (1.3 \pm 0.1) \times$   
143  $10^7 \text{ kg}$ . Considering the change in effective cross section before impact and after the fast-moving  
144 ejecta dissipated, Equation 3 in the Methods section results in an average dust radius  $\bar{a} \sim 1.7 \pm$   
145  $0.3 \text{ mm}$ .

146 We also estimate the particle radius in the observed coma by relating solar radiation  
147 pressure to the turn-around distance of the particles in the coma along the comet-Sun line, and

148 the bulk velocity of the particles,  $v_{ce}$  (detailed in the “Mass of the Ejecta” section of the Methods).  
149 It was found that particles reached distances  $d \sim 150 - 250$  km in the solar direction before turning  
150 around<sup>14</sup>. We, then find average dust radii  $\bar{a} \sim 2.8 \pm 0.3 - 3.8 \pm 0.4$  mm in the coma, corresponding  
151 to a mass range of  $m_{ce} \sim (1.3 - 2.2) \times 10^7$  kg, in good agreement with our estimate above.

152 In all scenarios, we find that while the impact led to a significant increase in apparent  
153 magnitude, the overall mass loss in the observed fast-moving ejecta plume or slower moving ejecta  
154 in the coma created by DART's impact into Dimorphos was not totally disruptive.

155 We also measure the color before, during, and after DART's impact into Dimorphos as  
156 seen in Figure 4 to show a significant reddening at the time of impact. The colors appear to return  
157 to their original color as the fast-moving ejecta plume dissipates. This initial reddening was also  
158 seen on 9P/Tempel 1 after the impact of NASA's *Deep Impact* spacecraft and was determined to  
159 be caused by different sized particles having a range of velocities, causing the particle size  
160 distribution and the ejecta optical depth to change over time<sup>15</sup>.

161 If the reddened color is interpreted as a proxy for material composition, we must consider  
162 this in the context of the colors of active and inactive small bodies in the solar system. Typically,  
163 active bodies appear bluer in color on average than their inactive counterparts, such as short-  
164 period comets versus Kuiper belt objects<sup>16</sup>. Some of these redder observed surface colors may be  
165 due to irradiation of organics<sup>17</sup>, which can efficiently mantle the surface of bodies like the Kuiper  
166 belt objects<sup>18,19</sup>. Additionally, in general, the highest velocity ejecta from an impact is sourced  
167 from the material closest to the site of impact<sup>20</sup>. The fast-moving ejecta plume may be more  
168 representative of the surficial material of Dimorphos than the material in the slower-moving  
169 coma. While much of the fine-grain surface regolith on Dimorphos has likely been depleted

170 through processes like electrostatic removal<sup>21</sup>, it is possible that the remaining small particles  
171 have experienced some irradiation. Spectra indicate the presence heterogeneity of surface  
172 materials on Didymos, with various concentrations of likely hypersthene with a grain radius  $a$   
173  $<25 \mu\text{m}$ , and olivine with a grain radius  $a <45 \mu\text{m}$ <sup>22</sup>. Lab simulations of space weathering showed  
174 that irradiation can cause significant reddening of olivine's reflectance spectrum<sup>23</sup>. We  
175 emphasize that these posed interpretations are a few of possibly many.

ACCELERATED ARTICLE PREVIEW

176 **References**

- 177 [1] Daly, R. T. *et al.* DART: An Autonomous Kinetic Impact into a Near-Earth Asteroid for  
178 Planetary Defense. *Nature* (**this issue**), (2023).
- 179 [2] Fahnestock, E. G., et al. Pre-encounter predictions of DART impact Ejecta behavior and  
180 observability. *Planet. Sci. J.*, **3**, 206. (2022).
- 181 [3] Richardson, D. C. *et al.* Predictions for the Dynamical States of the Didymos System  
182 before and after the Planned DART Impact. *Planet. Sci. J.* **3**, 157 (2022).
- 183 [4] [noirlab.edu/public/news/noirlab2223/](https://noirlab.edu/public/news/noirlab2223/)
- 184 [5] Jewitt, D. *et al.* Hubble Space Telescope Observations of Main-Belt Comet (596) Scheila.  
185 *Astrophys. J.*, **733**, L4 (2011).
- 186 [6] Bodewits, D. *et al.* Collisional Excavation of Asteroid (596) Scheila. *ApJ*, **733**, L3 (2011).
- 187 [7] Jewitt, D. The Active Asteroids. *Astron. J.*, **143**, 66 (2012).
- 188 [8] Braslau, D. Partitioning of energy in hypervelocity impact against loose sand targets. *J.*  
189 *Geophys. Res.*, **75**, 3987-3999 (1970).
- 190 [9] Gault, D. E. The partition of energy for hypervelocity impact craters formed in rock.  
191 In *Proc. Sixth Hypervelocity Impact Symp.* **2**, 419-456 (1963).
- 192 [10] Okeefe, J. D., & Ahrens, T. J. Impact-induced energy partitioning, melting, and  
193 vaporization on terrestrial planets. In *Lunar and Planetary Science Conference*  
194 *Proceedings*, **8**, 3357-3374, (1977).
- 195 [11] Naidu, S. P. *et al.* Radar observations and a physical model of binary near-Earth asteroid  
196 65803 Didymos, target of the DART mission. *Icarus* **348**, 113777 (2020).

- 197 [12] Zubko, E., *et al.* Expected Brightness of Ejecta Caused by the DART Impact. *Res. Notes*  
198 *AAS*, **6**, 186 (2022).
- 199 [13] Housen, K. R. and Holsapple, K. A. Ejecta from impact craters. *Icarus*, **211**, 856-875  
200 (2011).
- 201 [14] Li, J-Y. Ejecta from the DART-produced active asteroid Dimorphos. *Nature* (**this issue**),  
202 (2023).
- 203 [15] D. G. Schleicher, D. G. Photometry and Imaging Results for Comet 9P/Tempel 1 and Deep  
204 Impact: Gas Production rates, Postimpact Light Curves, and the Ejecta Plume Morphology.  
205 *Astron. J.*, **131**, 1130 (2006).
- 206 [16] Jewitt, D. Color Systematics of Comets and Related Bodies. *Astron. J.*, **150**, 201 (2015).
- 207 [17] Brunetto, R., *et al.* Modeling asteroid surfaces from observations and irradiation  
208 experiments: The case of 832 Karin. *Icarus*. **184**, 327-337 (2006).
- 209 [18] Cooper, J. F. Proton Irradiation of Centaur, Kuiper Belt, and Oort Cloud Objects at Plasma  
210 to Cosmic Ray Energy. *Earth, Moon, and Planets*, **92**, 261-277 (2003).
- 211 [19] M. E. Brown, M. E., *et al.* A Hypothesis for the Color Diversity of the Kuiper Belt.  
212 *Astrophys. J. Lett.*, **739**, L60 (2011).
- 213 [20] Melosh, H. J. Impact Cratering: A Geologic Process. *New York: Oxford University Press*  
214 (1989).
- 215 [21] Hsu, H.-W., *et al.* Fine-grained regolith loss on sub-km asteroids. *Nature Astronomy*, **6**,  
216 1043-1050 (2022).
- 217 [22] Ieva, S., *et al.* Spectral Rotational Characterization of the Didymos System prior to the  
218 DART Impact. *Planet. Sci. J.*, **3**, 183 (2022).

219 [23] Yamada, M., *et al.* Simulation of space weathering of planet-forming materials:  
220 Nanosecond pulse laser irradiation and proton implantation on olivine and pyroxene  
221 samples. *Earth Planets Space*, **51**, 1255-1265 (1999).

## 222 **Figure Legends**

223 **Figure 1. eVscope Observations of the Impact, Ejecta, and Tail.** Panels a-f show the initial  
224 ejecta plume from DART's impact into Dimorphos as observed from L'Étang-Salé, Réunion.  
225 Panel a shows Didymos before the DART impact. Panels b-f show Didymos after the DART  
226 impact. The compass and image scale in panel a applies to panels b-f as well. The fast-moving  
227 ejecta plume moves eastward on the plane of the sky and dissipates over time, from panels a to  
228 f. Panels g and h show two tails (~solar and ~anti-solar directions) developed from the ejecta  
229 produced by the DART spacecraft ~ 113.7 hours after impact into Dimorphos. The image in  
230 panel h is a zoomed-in version of the image in panel g. This image is a median stack of 1,205  
231 four-second exposures as observed from Nagahama, Japan. The two light blue arrows mark the  
232 two tails visible to an eVscope as visual aids.

233

234 **Figure 2. Apparent Magnitude of Didymos Before, During, and After Impact.** The light  
235 curve of the Didymos binary system on 26 September 2022 during the DART spacecraft's impact  
236 into Dimorphos as observed by three citizen astronomers located on Réunion Island using  
237 eVscopes. The dotted lines are the measured apparent magnitude before impact (bottom) and  
238 after the fast-moving ejecta dissipated after the impact (top). The shaded regions represent the  
239 standard deviation on the value of the dotted lines, and error bars represent sky background noise.

240 **Figure 3. Fading of Didymos After Impact.** The absolute magnitude of the Didymos system  
241 faded over time after the brightening due to DART’s impact into Dimorphos. The solid blue line  
242 is a weighted, linear fit to magnitudes measured from just after impact on 2022 Sep 26 through  
243 2022 Oct 25, after which measurements were consistent with the resting absolute magnitude.  
244 Some measurements between Oct 15 and 25 overlap the resting magnitude at the  $\sim 1\sigma$  level but  
245 others remain above it. Therefore, we consider the fading time may range between  $\sim 18$  and  $\sim 28$   
246 days after impact, with our best-fit model providing a fading time of  $23.7 \pm 0.7$  days. The value  
247 of the resting absolute magnitude is calculated from the pre-impact average apparent magnitude  
248 plotted in Figure 2. The error bars and shaded region represent the  $1\sigma$  measurement uncertainties.  
249 Prior to 2022 Oct 4, there are two outlying observations that resulted in measurements that were  
250 too faint due to poor weather conditions, and we therefore do not include these points in the fitted  
251 line.

252  
253 **Figure 4. Colors of Didymos Before, During, and After Impact.** Measured B-G (a), G-R (b),  
254 and B-R (c) colors of Didymos over time as observed from L'Étang-Salé, Réunion. Error bars  
255 represent the noise introduced by the sky background magnitude. It is apparent in panels a and c  
256 that the Didymos binary system became redder directly after the DART spacecraft impacted  
257 Dimorphos and that when the fast ejecta dissipated, the colors returned to their original colors.  
258 The G-R colors in panel b show no significant change in color during the time of impact.

## 259 **Methods**

### 260 **Observations**

261 The measurements in this work are derived from 23,240 images taken by 17 different  
262 eVsopes in the Unistellar network of eVsopes. At the time of this study, the Unistellar fleet of  
263 eVsopes contained three variations: the eVscope 1, eVscope eQuinox, and the eVscope 2. All  
264 eVsopes have 112 mm diameter primary mirrors. The eVscope 1 and eQuinox both utilize a  
265 Sony IMX224LQR sensor and have a  $37' \times 28'$  field of view and pixel scale of  $1.72''/\text{pix}$ , while  
266 the eVscope 2 utilizes a Sony IMX347LQR sensor and has a  $45' \times 34'$  field of view and pixel  
267 scale of  $1.33''/\text{pix}$ . The detectors have RGB photosensors arranged as Bayer filter matrices.  
268 Exposure times of individual images varied between observers from 1.0 to 4.0 s but remained  
269 constant throughout each individual data set. Images were taken consecutively over ranges of  
270 10 to 80 minutes. In this work, we report observations taken from 2022 Sep 26 through 2022  
271 Oct 31 UT. Over this time range, the observing parameters of Didymos ranged from geocentric  
272 distances of 0.076 to 0.109 au, heliocentric distances of 1.046 to 1.018 au and phase angles of  
273  $53.2^\circ$  to  $73.8^\circ$ . Figure 1 shows two of the tails that formed after impact as seen on 2022 Oct 1,  
274 when the position angle was  $60.4^\circ$  in the projected anti-solar direction and  $27.6^\circ$  in the  
275 projected anti-velocity direction. In each data set, the limiting magnitude is between 15 and 16  
276 magnitudes, except for the stacked image that shows the tails in Figure 1, which consists of  
277 1,250 four-second images. For this data set, we measure a  $3\sigma$  limiting magnitude of  $17.01 \pm$   
278  $0.03$ . We further summarize the observation circumstances in Extended Data Table 1.

## 279 **Aperture Photometry**

280 To measure the magnitude of Didymos in the images, we first reduce the data submitted  
281 by Unistellar citizen astronomers. Unistellar Citizen astronomers submit science images with  
282 their chosen parameters (as listed above) as well as dark frames for calibration which are recorded  
283 immediately after the science observations. The dark frames are median combined and subtracted  
284 from the science images. The Unistellar Network is currently not prompted to take flat frames to  
285 further calibrate the data. In general, we find the errors on photometric measurements are  
286 dominated by photon noise and sky rather than the lack of a flat-field correction. We also aim to  
287 keep Didymos in the middle of the detector when conducting observations to further mitigate the  
288 lack of a flat frame calibration. Before conducting aperture photometry, the science images are  
289 aligned and median-combined in time; however, the observations conducted during the DART  
290 impact displayed in Figure 2 were measured from images that were not stacked because of the  
291 speed of brightening upon impact. The photometry measurements on the observations conducted  
292 after the impact were conducted on median-combined images that vary from 17 to 30 images.  
293 The measurements are then averaged and plotted at the midpoint in time of the conducted  
294 observation. We choose an aperture radius of 13.6" (corresponding to 750 km at the distance of  
295 Didymos) through which we measure the flux. The PSF of Didymos after the impact depends on  
296 the dataset. Table 1 in Extended Data lists the average full width at half maximum (FWHM) of  
297 the gaussian-fitted PSFs of the stars in each dataset. The most egregious cases were due to out of  
298 focus eVsopes. We find the FWHM of the PSF of Didymos is  $\sim 9.0 \pm 1.0\%$  larger than that of  
299 the stellar PSFs. Our chosen aperture is large enough to measure all the flux from the Didymos  
300 system throughout all the submitted datasets. We subtract the flux of the sky background

301 measured through an annulus centered on the target that ranges from 22.21" to 30.75" in radius,  
302 corresponding to ~1218 km to ~1686 km at the distance of Didymos. We use stars in the field  
303 with known Gaia magnitudes to convert our instrumental flux values to apparent magnitudes,  
304  $m_V$ . These magnitudes are plotted in Figure 2. When measuring the magnitude before impact and  
305 after the fast-moving ejecta dissipated, we use observations from the eVscope in L'Étang-Salé,  
306 Réunion on 2022 Sep 26. This eVscope was able to reach the greatest sensitivities as it was  
307 contained in a protective dome that blocked wind and stray light.

308 To obtain the colors of the Didymos binary system, the color channels of the detectors  
309 must be isolated. In a Bayer filter matrix of blue (B), green (G), and red (R) photosensors, the  
310 first  $2 \times 2$  section of pixels is arranged as [R, G; G, B]. This pattern repeats to fill the size of the  
311 detector. We isolate each color channel based on this known pattern of the photosensors and  
312 conduct aperture photometry as described above. We calibrate the instrumental fluxes using  
313 calibrator stars with known Gaia magnitudes in the background of each image. We measure the  
314 aperture fluxes of those calibrator stars in each color channel and, combined with their known  
315 Gaia magnitudes, use them to convert the Didymos aperture fluxes in those channels to B, G, and  
316 R magnitudes<sup>24</sup>. We plot the resulting B-G, G-R, and B-R colors, the B-G and B-R colors in  
317 Figure 4.

### 318 **Mass of the Ejecta**

319 Apparent magnitudes  $m_V$  are converted to absolute magnitudes,  $H_V$ , which represents  
320 the magnitude of the object with heliocentric and geocentric distance ( $r_H$  and  $\Delta$  respectively) of  
321 1 au and at phase angle,  $\alpha = 0^\circ$ . The correction is

322 
$$H_V = m_V - 5 \log_{10}(r_H \Delta) - \beta \alpha \quad (1)$$

323 where  $\beta \alpha$  is the phase function that represents the dependence on sunlight scattering by the dust  
 324 particle at an angle  $\alpha$  in degrees. We assume a linear phase function with phase coefficient,  $\beta =$   
 325 0.035, a typical value for S-type asteroids like Didymos<sup>25, 26, 27, 28, 29</sup>. With this, our measured  
 326 absolute magnitude before the impact of  $H_V = 18.12 \pm 0.11$  agrees with past measurements of  
 327  $H_V = 18.16 \pm 0.04$  of the binary system<sup>30</sup>. Absolute magnitudes are plotted in Figure 3. Next, we  
 328 estimate the effective cross sections with

329 
$$C_e = \frac{\pi(2.25 \times 10^{16})}{p_v} 10^{-0.4[H_V - V_\odot]} \quad (2)$$

330 where  $p_v \sim 0.15 \pm 0.02$  is the albedo of the Didymos system measured by the DRACO  
 331 camera<sup>1</sup>,  $H_V$  is the absolute magnitude we measure for the Didymos system, and  $V_\odot \sim -26.77$  is  
 332 the apparent magnitude of the Sun. For Didymos, we find an effective scattering cross section  $C_e$   
 333  $\sim 0.53 \pm 0.06 \text{ km}^2$  before impact,  $C_e \sim 4.35 \pm 0.13 \text{ km}^2$  at Didymos' peak in brightness just after  
 334 impact, and  $C_e \sim 2.17 \pm 0.09 \text{ km}^2$  after the fast-moving ejecta moved out of the photometric  
 335 aperture. A cross section  $C_e \sim 0.53 \pm 0.06 \text{ km}^2$  implies an effective radius  $r_e \sim 411 \pm 22 \text{ m}$ , which  
 336 is consistent with previous radar measurements of Didymos finding a volume equivalent radius  
 337 of  $r_e \sim 390 \pm 15 \text{ m}$ <sup>11</sup>. The mass is related to the effective cross section by

338 
$$M_e = \frac{4}{3} \rho \bar{a} C_e \quad (3)$$

339 where  $\rho \sim 2400 \pm 250 \text{ kg m}^{-3}$  is the bulk density of the Didymos system<sup>1</sup>, and we adopt  $\bar{a} =$   
 340  $\sqrt{a_{min} a_{max}}$  for the mean dust radius amongst particles having a size range  $a_{min} \leq a \leq a_{max}$ .

341 We examine particles with mean radii  $\bar{a} \sim 0.1 - 1 \text{ } \mu\text{m}$  in the fast-moving ejecta as was found for

342 the ejecta in impacted asteroid Scheila<sup>5</sup>. The change in effective cross section measured at peak  
 343 brightness and at the leveled brightness after the fast-moving ejecta dissipated then allows us to  
 344 measure the change in mass, or the mass contained in the fast-moving ejecta plume with  
 345 Equation 3. We do the same for the mass lost in the coma of slower moving particles by  
 346 examining the change in cross section from before impact and after impact, when the fast-  
 347 moving ejecta dissipated from the photometric aperture. However, instead of assuming a dust  
 348 size within the coma, we estimate the dust size in two ways. First, we estimate the mass in the  
 349 coma based on the fading time of Didymos after impact and the speed of the particles through a  
 350 process explained in the following section. Equation 3 then gives an estimate on the average  
 351 dust radius. We also estimate the dust radius by connecting the distance a particle can reach in  
 352 the Solar direction before being turned around by Solar radiation pressure to its initial speed  
 353 using

$$354 \quad B = \frac{u^2 r_H^2}{2GM_\odot \ell} \quad (4)$$

355 where  $B$  is a dimensionless radiation pressure factor,  $G = 6.67 \times 10^{-11} \text{ m}^3 \text{ kg}^{-1} \text{ s}^{-2}$  is the  
 356 gravitation constant,  $M$  is the mass of the Sun,  $r_H \sim 1.04 \text{ AU}$  is the heliocentric distance of  
 357 Dimorphos on 2022 Oct 1, when the turn-around distance was measured to reach  $\ell \sim 150\text{-}200$   
 358  $\text{km}^{14}$ , and  $u$  is the initial velocity of the particles which we measure as  $u \sim v_{ce} \sim 0.37 \pm 0.01$   
 359  $\text{m s}^{-1}$  from the fading rate of Didymos.  $B$  is the ratio of acceleration due to solar radiation  
 360 pressure to the acceleration due to solar gravity expressed as

$$361 \quad B = \frac{KQ_{pr}}{\rho a} \quad (5)$$

362 where  $K = 5.7 \times 10^{-4} \text{ kg m}^{-2}$  is a constant,  $Q_{pr}$  is the radiation pressure coefficient often assume  
363 to be 1,  $\rho$  is the particle density, and we examine the average dust  $a = \bar{a}$ . Again, we examine  
364 dust densities equivalent to the bulk density of the Didymos system<sup>1</sup>. Assuming  $\rho \sim 2400 \pm 250$   
365  $\text{kg m}^{-3}$  gives  $B \sim (0.24 \pm 0.02) / \bar{a}$  microns. We point out that using a particle  $\rho \sim 3480 \pm 80 \text{ kg}$   
366  $\text{m}^{-3}$ , which is the average density of LL ordinary chondrite material<sup>31</sup> as associated with S-type  
367 asteroid Didymos<sup>32</sup>, also result in mm size particles corresponding to masses within the range  
368 we estimate when assuming  $\rho \sim 2400 \pm 250 \text{ kg m}^{-3}$ .

### 369 **Speed and Energy of the Ejected Dust**

370 To estimate the energy carried by the mass in that fast-moving ejecta plume and slower  
371 moving coma, we obtain their speeds. The fast-moving ejecta can be measured visually,  
372 following the plume on the detector over time. Additionally, we measure the crossing time,  $t_c$ ,  
373 of the particles in the photometric aperture. This is the time between the moment of impact and  
374 the moment the magnitude settled to  $m_v = 12.96 \pm 0.04$ . We determine the peak time and  
375 dissipation time of the fast-moving ejecta by analyzing the magnitudes binned into rolling bins  
376 of 5 images to determine peak time and 15 images for the settling time. We then choose times  
377 when the residuals were within the respective measured errors on the peak magnitude and  
378 magnitude after fast-moving ejecta dissipation. We find a crossing time  $t_c \sim 775 \pm 40 \text{ s}$  over a  
379 photometric aperture radius of  $13.67''$ , which is equivalent to  $\sim 750 \text{ km}$  at the distance of  
380 Didymos. Therefore, we obtain a speed of  $v \sim 970 \pm 50 \text{ m s}^{-1}$ .

381 In the slower moving ejecta that makes up the coma, we estimate the particle speed from  
382 the fading time of Didymos after impact. This is the time between the moment of impact and

383 the moment the magnitude increased back to Didymos' original absolute magnitude,  $H_V = 18.12$   
384  $\pm 0.11$ . Then, assuming equal projectile and target densities, we make a simple estimation of the  
385 mass of the ejecta  $m_e$  by the impact relation

$$386 \quad m_e = A * M_p \left( \frac{u}{U_p} \right)^s \quad (6)$$

387 where  $U_p \sim 6144.9 \pm 0.3$  is the impact speed of the DART spacecraft<sup>1</sup>,  $M_p \sim 579.4 \pm 0.7$  is the  
388 mass of the DART spacecraft on impact<sup>1</sup>,  $u \sim v_{ce} \sim 0.37 \pm 0.01 \text{ m s}^{-1}$  is the bulk velocity of the  
389 particles in the ejecta, and for consistency with past works  $A = 0.01$  is a constant and  $s$  is an  
390 index that that we approximate to  $s = -1.5$  but depends on the material<sup>7, 13</sup>. The density of  
391 Dimorphos is assumed to be the same as the bulk density of the Didymos system in the  
392 calculations, however we emphasize that the density of Dimorphos alone is not measured. The  
393 density of the main body of the DART spacecraft (without the solar panels) was  $\sim 270 \text{ kg m}^{-3}$   
394 at impact time<sup>33</sup>. For the sake of this simple approximation, we take the densities of the  
395 spacecraft and Dimorphos to be similar enough, because we expect lower densities with  
396 decreasing diameter for S-type asteroids<sup>34</sup> and that the Spacecraft was stopped by Dimorphos  
397 rather than flying straight through it. We also emphasize that this approximation comes with the  
398 caveat that impact physics on small asteroids are still not well-understood, so this impact  
399 relation serves as a rough estimate<sup>34</sup>.

400 With the estimated masses,  $m$  and speeds,  $v$  of the ejecta, we can estimate the kinetic energy,  
401  $E_K$  carried by the initial fast-moving ejecta as well as the coma by  $KE = (1/2) mv^2$ . As a tool  
402 to choose appropriate dust size test-cases, we compared the estimated kinetic energies to the  
403 kinetic energy introduced by the DART spacecraft where mass on impact is  $M_p \sim 579.4 \pm$

404 0.7 kg and velocity on impact is  $v = U_p \sim 6144.9 \pm 0.3 \text{ m s}^{-1}$ . We also compare this to the  
405 orbital energy,  $E_O$  of Dimorphos around Didymos before and after the orbital period change of -  
406  $33.0 \pm 1.0 \text{ minutes}^{35}$  using

$$407 \quad E_O = \frac{-GM_{Did}m_{Dim}}{2r} \quad (7)$$

408 where  $M_{Did} \sim 5.6 \pm 0.5 \times 10^{11} \text{ kg}$ ,  $m_{Dim} \sim 4.3 \times 10^9 \text{ kg}$ , and  $r$  is the semi-major axis of the  
409 orbit of Dimorphos around Didymos<sup>1,36</sup>. Before the impact, the semi-major axis was measured  
410 to be  $r = 1.206 \pm 0.035 \text{ km}^1$ . We can estimate the original orbital energy of Dimorphos to be  
411  $E_O \sim -(6.6 \pm 0.6) \times 10^7 \text{ J}$ . With the orbital period decrease, Kepler's third law gives a new  
412 semimajor axis of  $r \sim 1.2 \pm 0.1 \text{ km}$  resulting in a change of orbital energy of  $\Delta E_O \sim (2.1 \pm$   
413  $0.6) \times 10^6 \text{ J}$ . These simple approximations are sufficient for the scope of this work, which  
414 aims to use these estimates as a means of providing a check on the reasonability of the  
415 estimated masses of the ejecta.

## 416 **Data Availability**

417 The Unistellar network of citizen astronomers have the option to upload their FITS  
418 images to an AWS server rented by the Unistellar corporation. This data is then available upon  
419 request. The resulting photometry used in the data analyses are made available on the  
420 corresponding author's public GitHub repository in the form of CSV files corresponding to the  
421 figures and extended data table. The repository also contains the FITS images used in Figure 1.  
422 The data is located in the corresponding author's public GitHub repository  
423 ([https://github.com/Ariel-Graykowski/DART\\_Unistellar](https://github.com/Ariel-Graykowski/DART_Unistellar))<sup>37</sup>.

424 **Code Availability**

425           The SETI/Unistellar pipeline used to dark-subtract and stack the astronomical images  
426 and conduct aperture photometry is currently located on Unistellar's private GitHub. These  
427 codes are available upon request. Python codes used to create the figures and conduct the main  
428 data analysis are located in the corresponding author's public GitHub repository  
429 ([https://github.com/Ariel-Graykowski/DART\\_Unistellar](https://github.com/Ariel-Graykowski/DART_Unistellar))<sup>37</sup>.

ACCELERATED ARTICLE PREVIEW

430 **Methods References**

- 431 [24] Cardiel, N., *et al.* RGB photometric calibration of 15 million Gaia stars. *Monthly Notices of*  
432 *the Royal Astronomical Society*, **507**, 318-329 (2021).
- 433 [25] Veverka, J. The Physical Meaning of Phase Coefficients. *International Astronomical*  
434 *Union Colloquium*, **12**, 79-90 (1971).
- 435 [26] Grehels, T. & Tedesco, E. F. Minor planets and related objects. XXVIII-Asteroid  
436 magnitudes and phase relations. *Astron, J*, **84**, 1079-1087 (1979).
- 437 [27] Schober, H. J. Rotation Period of 234 Barbara, a Further Slowly Spinning Asteroid.  
438 *Astronomy and Astrophysics*, **96**, 302-305 (1981).
- 439 [28] De Leon, J., *et al.* Observations, compositional, and physical characterization of near-Earth  
440 and Mars-crosser asteroids from a spectroscopic survey. *Astronomy and Astrophysics*, **517**,  
441 A23 (2010).
- 442 [29] Cheng, A. F., *et al.* AIDA DART asteroid deflection test: Planetary defense and science  
443 objectives. *Planet. Space Sci.* **157**, 104–115 (2018).
- 444 [30] Pravec, P., *et al.* Photometric Observations of the Binary Near-Earth Asteroid (65803)  
445 Didymos in 2015–2021 Prior to DART Impact. *Planet. Sci. J.*, **3**, 175 (2022).
- 446 [31] Britt, D. T., & Consolmagno, G. J. S. J. Stony meteorite porosities and densities: A review  
447 of the data through 2001. *Meteoritics & Planetary Science*, **38**, 1161-1180 (2003).
- 448 [32] Dunn, T. L., *et al.* Mineralogies and source regions of near-Earth asteroids. *Icarus*, **222**,  
449 273-282 (2013).
- 450 [33] Rainey, E. S. G., *et al.* Impact modeling for the Double Asteroid Redirection Test (DART)  
451 mission. *Int. J. Impact Eng.* **142**, 103528 (2020).

452 [34] Carry, B. Density of asteroids. *Planet. Space. Sci.*, **73**, 98-118 (2012).  
453 [35] Cheng, A., *et al.* Momentum Transfer from the DART Mission Kinetic Impact on Asteroid  
454 Dimorphos. *Nature* (**this issue**), (2023).  
455 [36] Fang, J. & Margot, J.-L. Near-Earth Binaries and Triples: Origin and Evolution of Spin-  
456 Orbital Properties. *Astron. J.*, **143**, 24 (2011).  
457 [37] Graykowski, A. Ariel-Graykowski/DART\_Unistellar: DART Unistellar (v1.0.0). Zenodo.  
458 <https://doi.org/10.5281/zenodo.7613581> (2023).

## 459 **Inclusion & Ethics**

460 Citizen astronomers, who are listed as co-authors, voluntarily observed this event and  
461 uploaded their data to an Amazon Web Services (AWS) server rented by the Unistellar  
462 Corporation. The analyses presented in this work were conducted locally at the SETI Institute,  
463 while the observations used in this work were conducted by citizen astronomers globally. This  
464 global network of eVscopes was a necessary tool to coordinate the proper timing and location to  
465 observe the DART impact and to continuously monitor the Didymos system over time.

## 466 **Acknowledgements**

467 This work was supported by a generous donation from the Gordon and Betty Moore  
468 Foundation. We thank Julie Bellerose for their communication on the observed timing of the  
469 DART impact. We thank the anonymous referees for reading the manuscript and providing  
470 helpful comments.

## 471 **Author Contributions**

472 A. G., R. A. L., and F. M. initiated this work. F. M. envisioned and organized the  
473 contribution of Unistellar network for the observations of the DART impact. A. G. and R. A. L.  
474 conducted photometric measurements on the images. A. G. led the analysis of the photometric  
475 datasets and R. A. L., F. M. provided significant contribution. R. A. L., F. M., D. C., P. A. D.,  
476 T. M. E., D. O’C. P., L. A. S. contributed to the interpretation, discussion, and the writing as  
477 well. F. M., A. M., L. M., and A. B. contributed to the creation of the Unistellar network. G. B.  
478 contributed to the establishment of the photometric pipeline. T. M. P. contributed to discussion  
479 of impact physics. P. H. (1), M. L., B. P., C. C., S. M., D. C. O., and R. W. contributed  
480 observations of Didymos taken before, during and after the impact of DART. M. M., K. F., T.  
481 G., B. G., P. H. (2), S. I., R. K., M. P., J. R., D. A. R., M. R., M. S., J-P. T., S. W., W-C. Y., and  
482 P. G. contributed observations of Didymos in the weeks following the impact in this work. M.  
483 C., K. G., R. J., D. J., S. K., M. L., J. W. P., B. A. S., and I. M. T. contributed observations of  
484 Didymos before the DART impact, which were used to prepare observation parameters for  
485 impact, and prepare the analyses that were used in this paper.

## 486 **Competing Interests**

487 The authors declare no competing interests.

## 488 **Additional Information**

489 Correspondence should be addressed to Dr. Ariel Graykowski ([agraykowski@SETI.org](mailto:agraykowski@SETI.org))

490

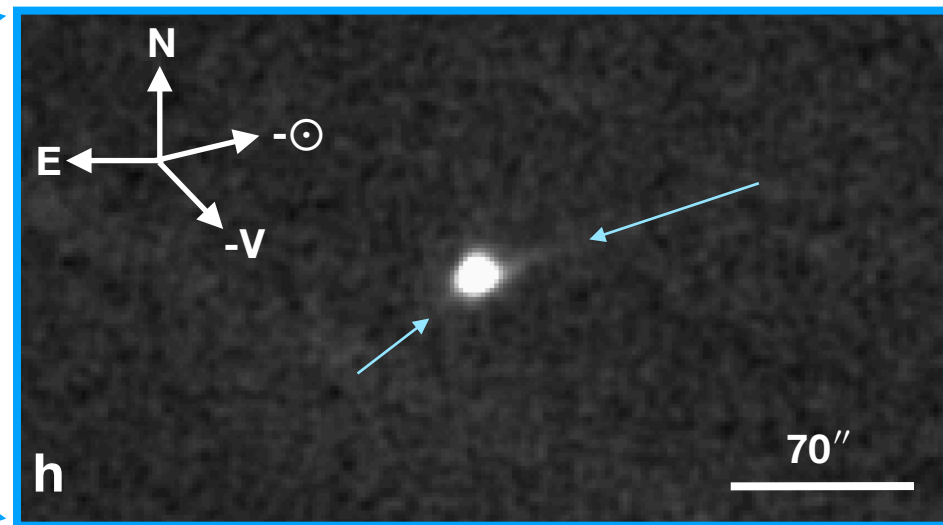
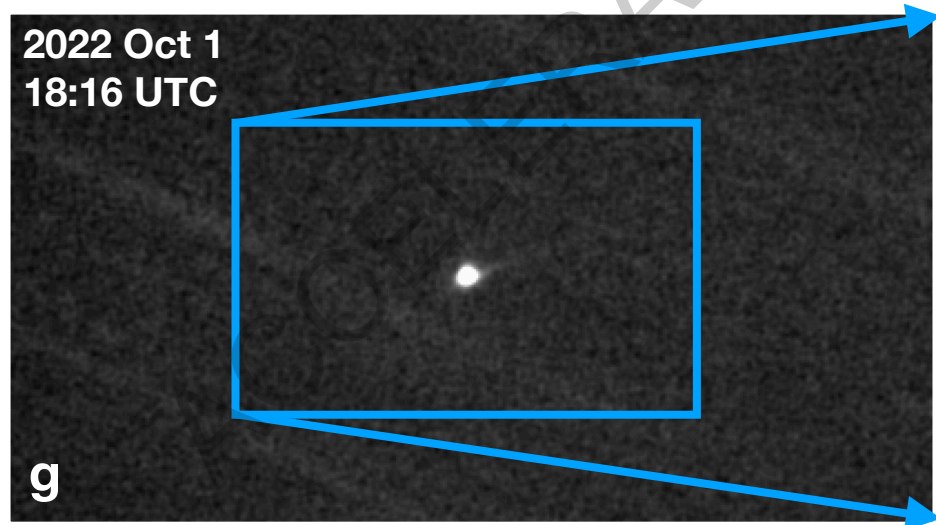
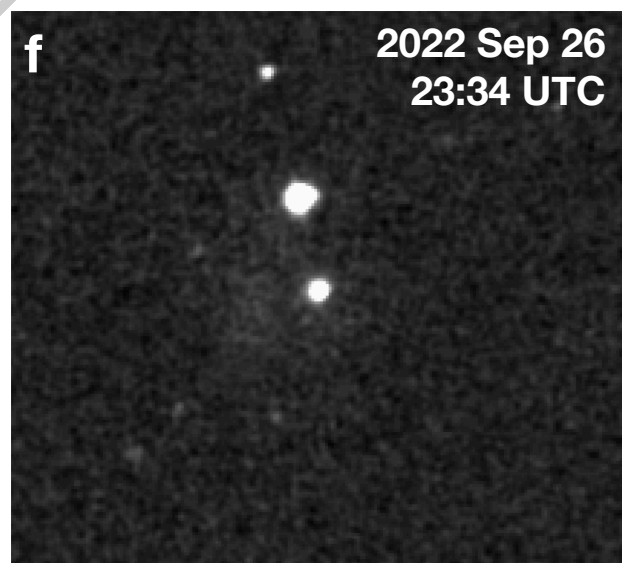
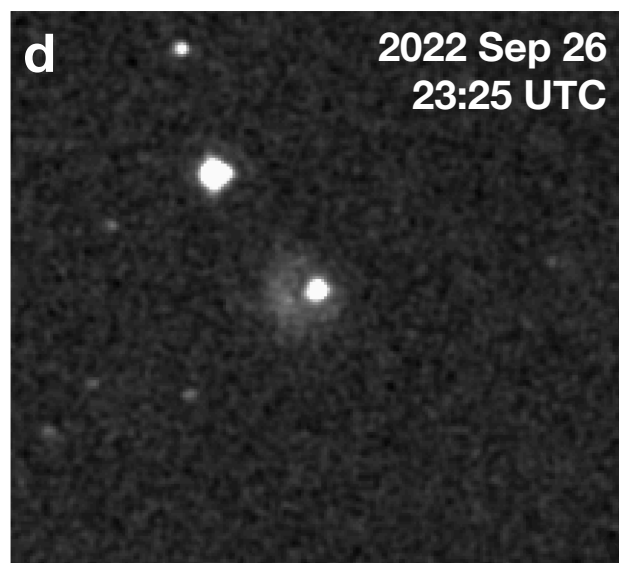
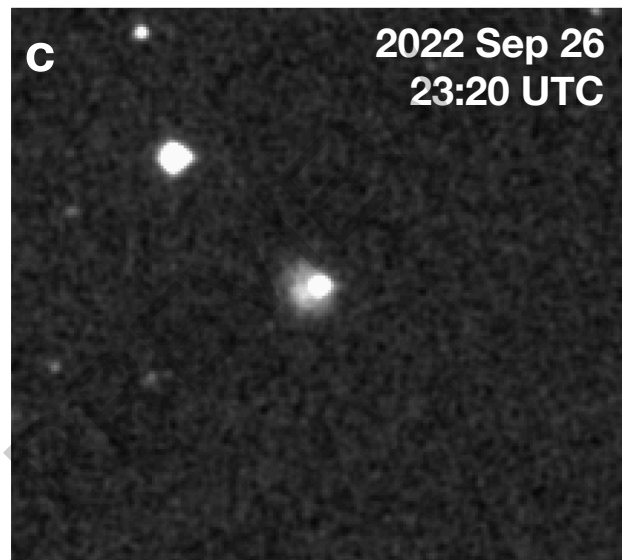
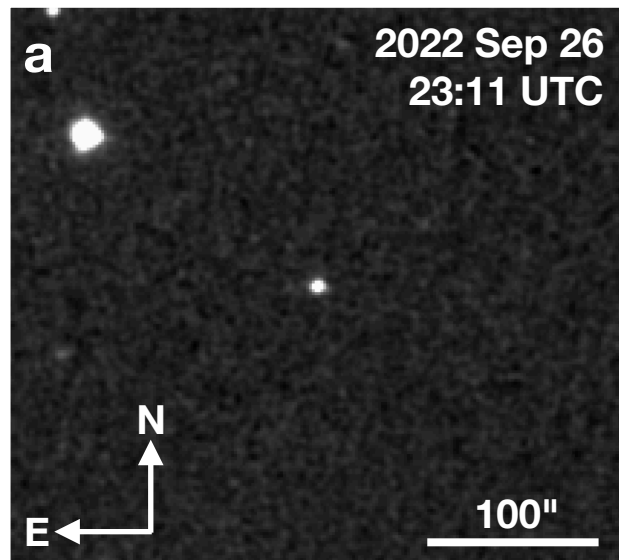
491

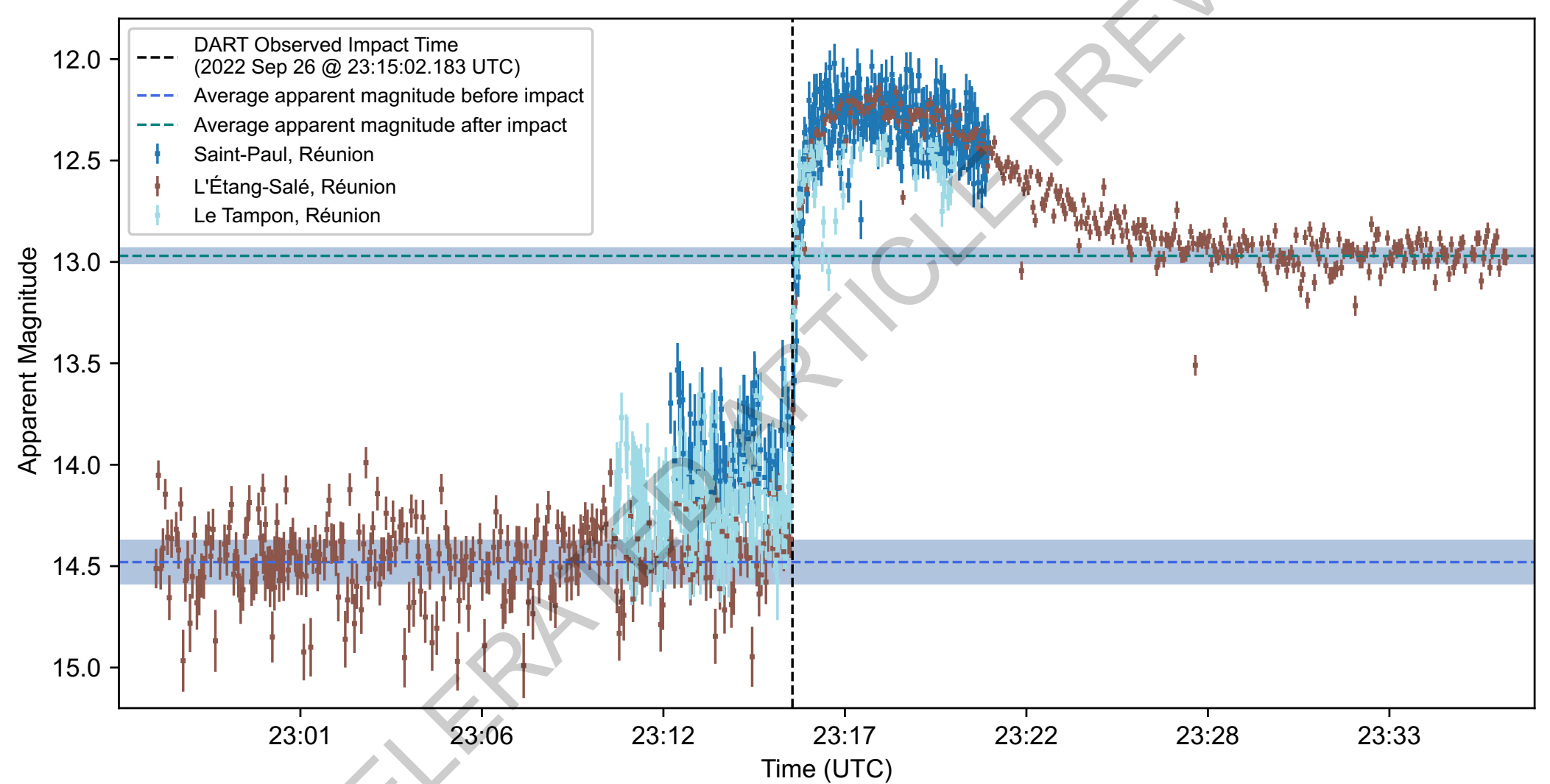
492

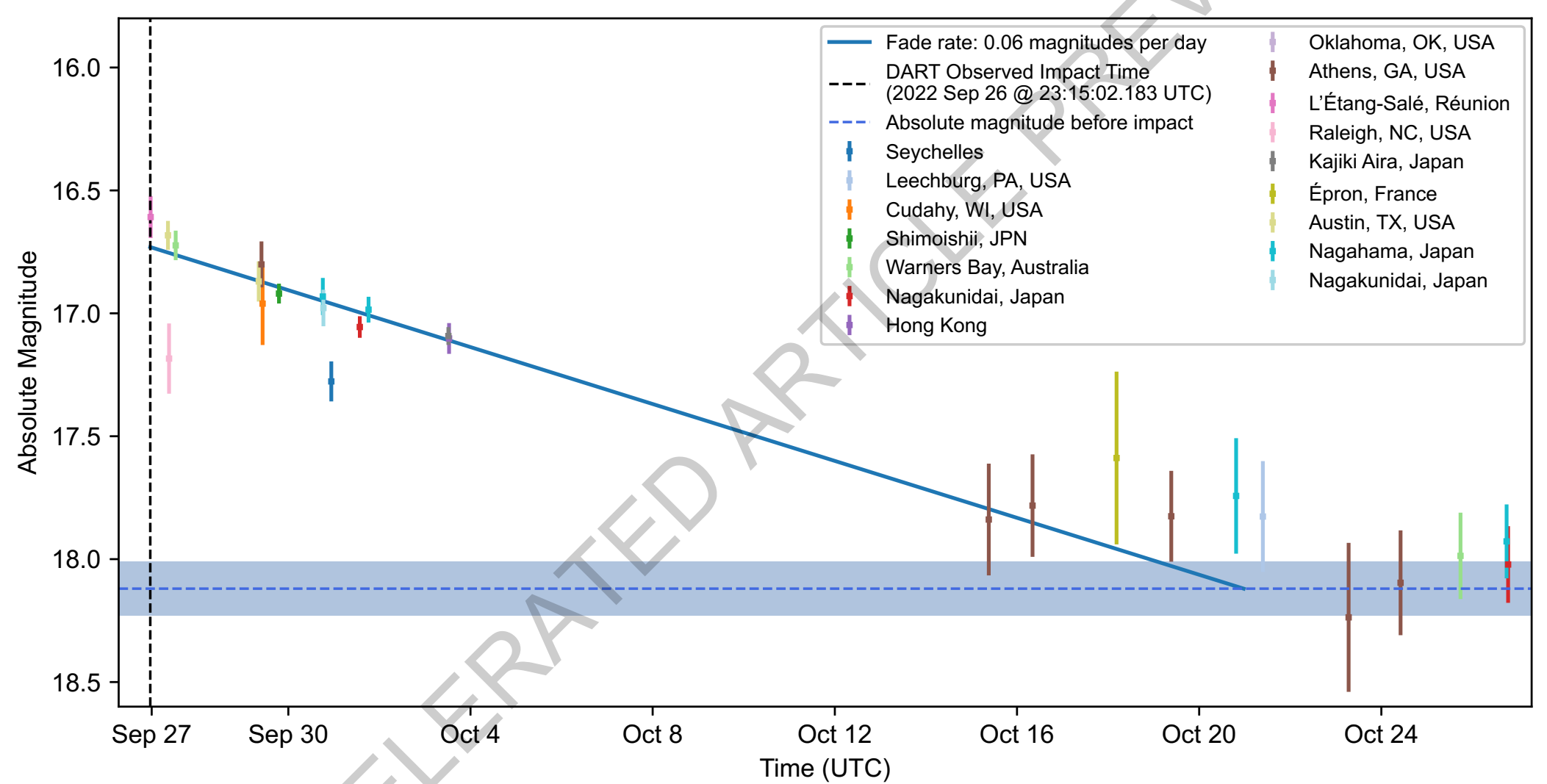
493 **Extended Data**

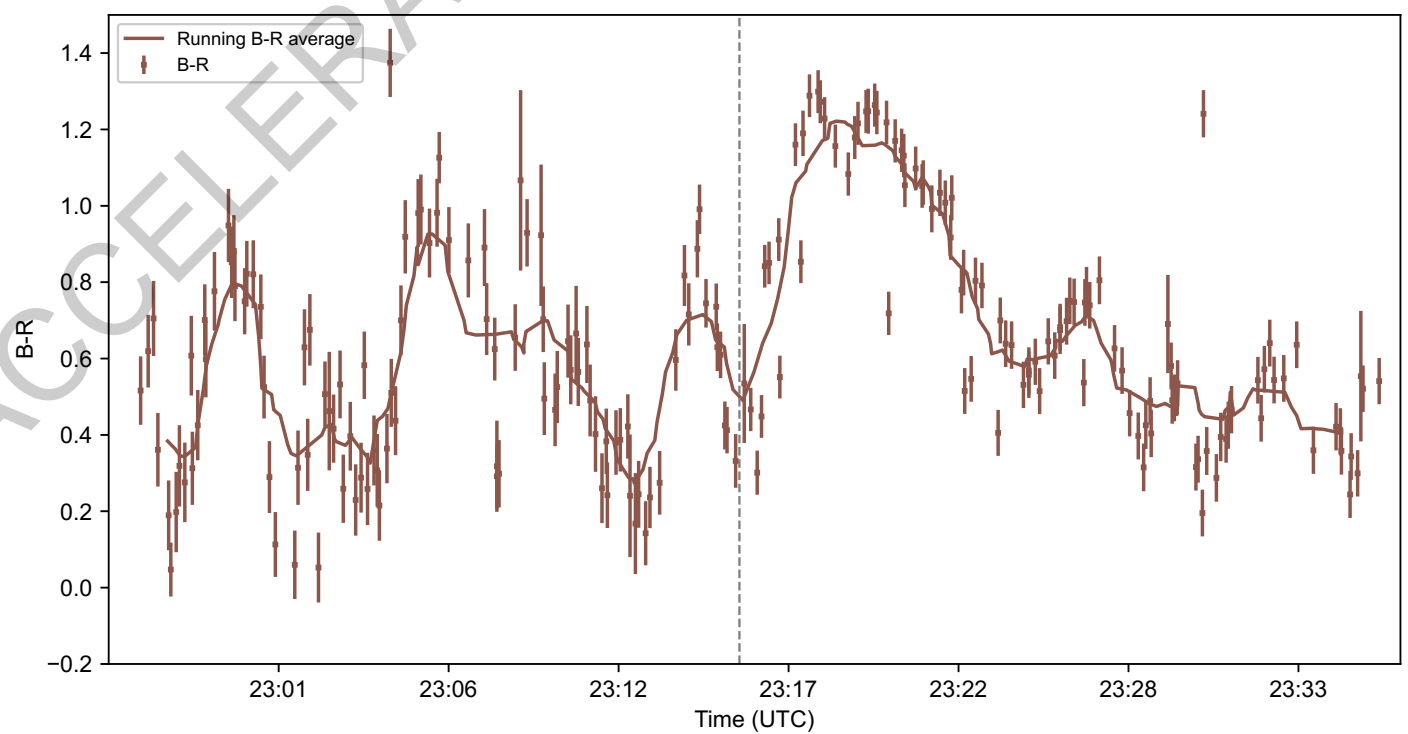
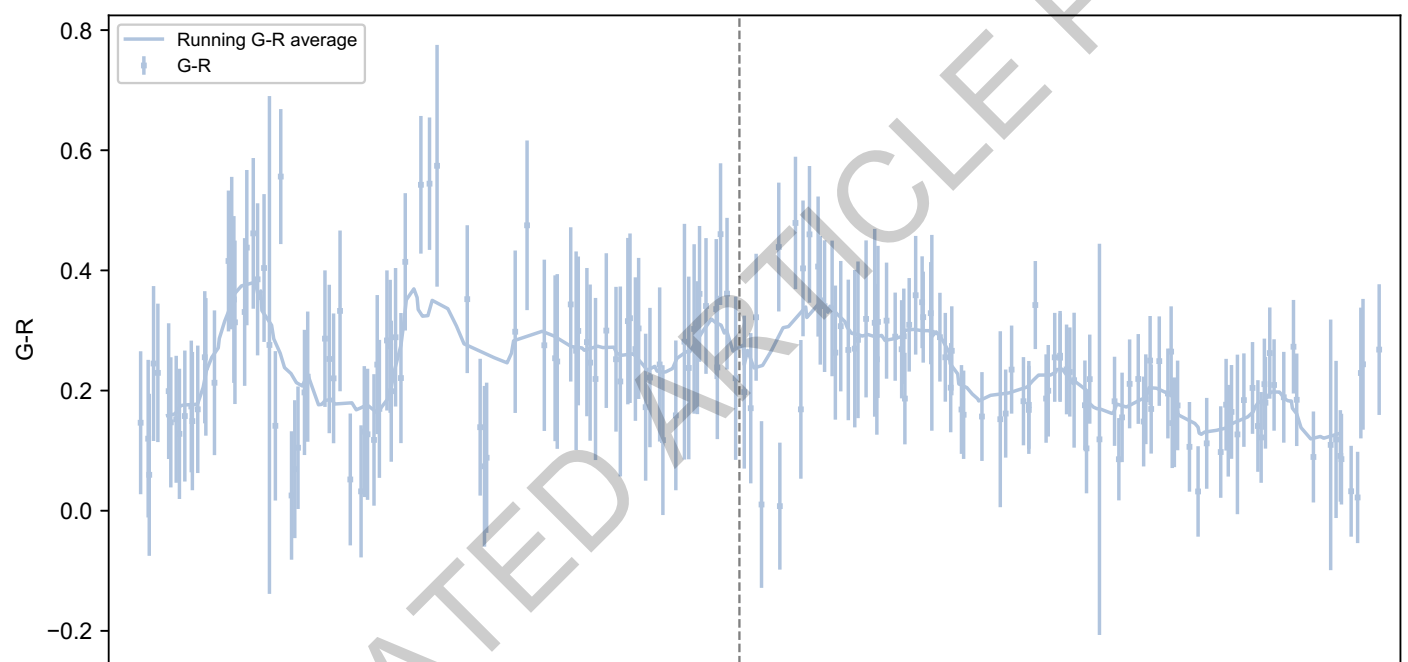
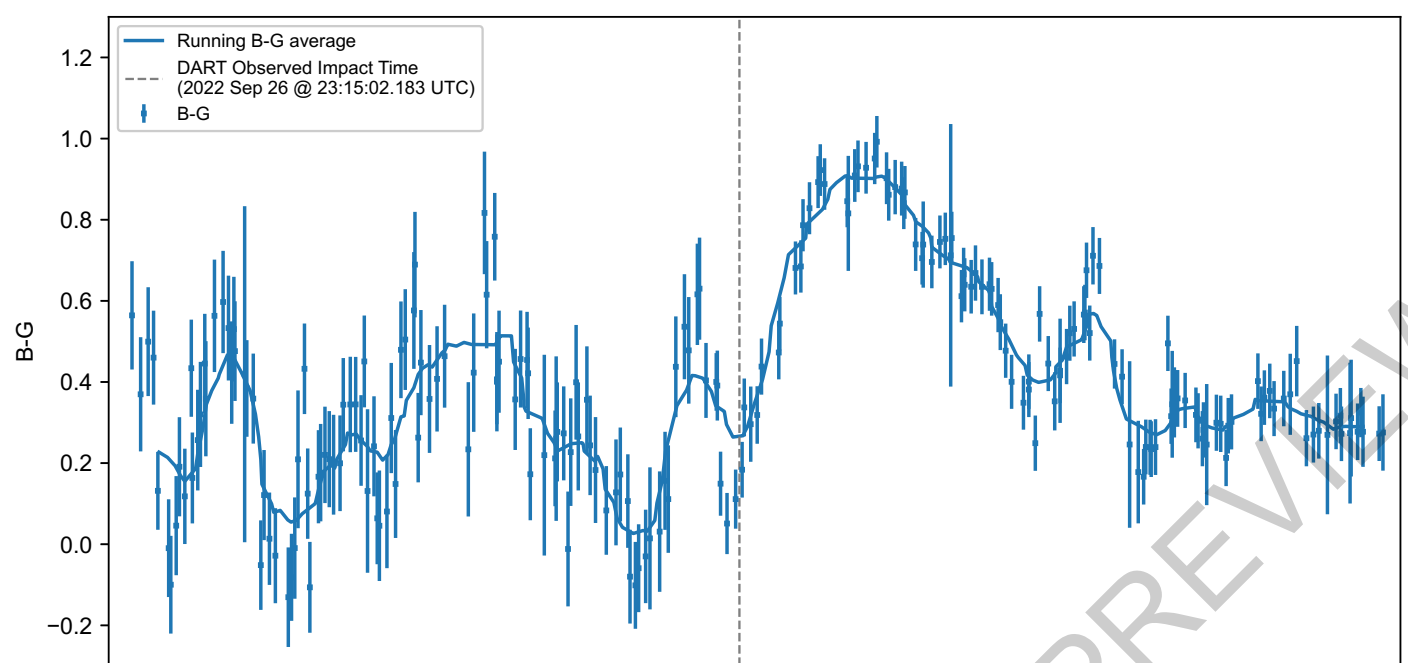
494 **Extended Data Table 1. Summary of observations.** Listed are the observations used in the  
495 above analyses from 2022 Sep 2022 to 30 Oct 2022. Observations were conducted by citizen  
496 astronomers across the World. The FWHM of the point spread function (PSF) of the stars is  
497 representative of the average “seeing” measured in each set of observations.

ACCELERATED ARTICLE PREVIEW









| Observer Initials | Observation start time (UTC) | Duration (min) | Location               | Exposure time (s) | # Frames | PSF FWHM (arcsec) |
|-------------------|------------------------------|----------------|------------------------|-------------------|----------|-------------------|
| P. H.(1)          | 2022 Sep 26 23:09:49         | 10             | Le Tampon, Réunion     | 1                 | 596      | 7.0 ± 0.4         |
| B. P.             | 2022 Sep 26 22:54:32         | 40             | L'Étang-Salé, Réunion  | 4                 | 624      | 6.29 ± 2.0        |
| M. L.             | 2022 Sep 26 23:10:45         | 10             | Saint Paul, Réunion    | 1                 | 597      | 5.9 ± 0.4         |
| M. P.             | 2022 Sep 27 08:10:07         | 50             | Austin, TX, USA        | 4                 | 759      | 18 ± 2.0          |
| S. W              | 2022 Sep 27 09:04:06         | 10             | Raleigh, NC, USA       | 4                 | 103      | 5.9 ± 0.2         |
| D. R.             | 2022 Sep 27 11:39:57         | 80             | Warners Bay, Australia | 4                 | 1059     | 5.6 ± 0.2         |
| M. P.             | 2022 Sep 29 08:03:06         | 40             | Austin, TX, USA        | 4                 | 568      | 10.26 ± 2.5       |
| J. R.             | 2022 Sep 28 08:47:46         | 180            | Athens, GA, USA        | 4                 | 1243     | 13.6 ± 0.4        |
| M. R.             | 2022 Sep 29 10:08:40         | 40             | Cudahy, WI, USA        | 4                 | 193      | 9.3 ± 0.4         |
| M. S.             | 2022 Sep 29 18:20:08         | 90             | Shimoishii, Japan      | 4                 | 1279     | 8.6 ± 0.3         |
| T. G.             | 2022 Sep 30 17:30:08         | 80             | Nagahama, Japan        | 4                 | 1231     | 3.9 ± 0.6         |
| K. F.             | 2022 Sep 30 17:55:15         | 110            | Nagakunidai, Japan     | 4                 | 1557     | 6.0 ± 0.4         |
| J.-P. T.          | 2022 Sep 30 22:36:44         | 6              | Seychelles             | 4                 | 95       | 4.4 ± 0.7         |
| T. G.             | 2022 Oct 01 16:55:38         | 120            | Nagahama, Japan        | 4                 | 1217     | 6.8 ± 0.4         |
| K. F.             | 2022 Oct 01 17:25:11         | 80             | Nagakunidai, Japan     | 4                 | 866      | 6.3 ± 0.35        |
| R. K.             | 2022 Oct 03 15:58:01         | 90             | Kajiki Aira, Japan     | 4                 | 578      | 4.1 ± 0.6         |
| W.-C. Y.          | 2022 Oct 03 16:20:05         | 220            | Hong Kong              | 4                 | 1345     | 3.7 ± 0.5         |
| J. R.             | 2022 Oct 14 08:54:15         | 30             | Athens, GA, USA        | 4                 | 425      | 13.4 ± 1.5        |
| J. R.             | 2022 Oct 15 07:54:53         | 30             | Athens, GA, USA        | 4                 | 468      | 5.7 ± 0.3         |
| B. G.             | 2022 Oct 17 03:29:54         | 110            | Épron, France          | 4                 | 1425     | 5.2 ± 0.5         |
| J. R.             | 2022 Oct 18 09:03:07         | 30             | Athens, GA, US         | 4                 | 176      | 5.1 ± 0.5         |
| K. F.             | 2022 Oct 20 19:01:10         | 40             | Nagakunidai, Japan     | 4                 | 561      | 6.8 ± 1.0         |
| P. H. (2)         | 2022 Oct 20 08:38:31         | 130            | Leechburg, PA, USA     | 4                 | 1871     | 7.3 ± 0.8         |
| J. R.             | 2022 Oct 22 06:32:53         | 30             | Athens, GA, USA        | 4                 | 469      | 5.4 ± 0.5         |
| J. R.             | 2022 Oct 23 09:52:59         | 30             | Athens, GA, USA        | 4                 | 469      | 4.2 ± 0.4         |
| D. A. R.          | 2022 Oct 25 17:25:51         | 40             | Warners Bay, Australia | 4                 | 457      | 5.9 ± 0.2         |
| T. G.             | 2022 Oct 26 17:51:37         | 30             | Nagahama, Japan        | 4                 | 481      | 4.9 ± 0.2         |
| K. F.             | 2022 Oct 26 18:28:15         | 40             | Nagakunidai, Japan     | 4                 | 658      | 5.9 ± 0.4         |
| M. M.             | 2022 Oct 30 06:45:23         | 130            | Oklahoma City, OK, USA | 4                 | 1869     | 5.7 ± 0.6         |

**Extended Data Table 1**